Algorithm for Three-Dimensional Ionospheric Radio Tomography Based on GNSS Data

V. M. Artemiev[a], P. A. Khmarski[a, *], and A. O. Naumov[a]

[a] Institute of Applied Physics, National Academy of Sciences of Belarus, Minsk, Republic of Belarus
***e-mail: pierre2009@mail.ru**

Abstract—The paper describes the design of an algorithm for three-dimensional radio tomography of electron concentration in the ionosphere based on the GNSS data. Simulation data are used to describe the algebraic reconstruction techniques underlying the algorithm design; also considered are the methods taking into account a priori information as well as the approaches to optimization of parameters of these algebraic methods. The results of the experimental ionospheric reconstruction obtained with the use of the data from the precise positioning satellite system of the Republic of Belarus are presented.

INTRODUCTION

The ionosphere is a highly ionized layer of the Earth's atmosphere, the state of which plays an important role in radio communications, radio navigation and various systems using electromagnetic waves [1, 2]. Reliable information on the three-dimensional (3D) structure of the electron concentration in the ionosphere makes it possible to improve the accuracy of positioning and navigation, as well as to provide more reliable short-wave radio communications in conditions of ionosphere variability [3–9].

Professor V.E. Kunitsyn, together with his students, made a significant contribution to the development of ionospheric radio tomography (IRT) techniques. In his works [1, 10–12], he proposed effective algorithms for IRT based on satellite data. The results he obtained have become the basis for a modern approach to 3D reconstruction of electron concentration distribution, which has been actively developing in recent decades.

The advent of the Global Navigation Satellite System (GNSS) has provided convenient access to a vast network of satellites emitting signals of different frequencies that interact with the ionosphere while passing through it [1–3, 7, 9, 13–16]. Such data formed the basis for numerous techniques of 3D IRT of electron concentration fields in the ionosphere, primarily based on various iterative algebraic reconstruction algorithms [17–20]. For example, IDA3D (Ionospheric Data Assimilation Three-Dimensional), an ionospheric objective analysis algorithm presented in [21], has successfully demonstrated a multisensor approach to the reconstruction of 3D models. An original approach to testing IRT techniques based on mathematical simulation is proposed in [22]. The review [23] is devoted to the history of the development of ionospheric reconstruction methods; it also describes the current state and prospects for using multi-instrument approaches to the reconstruction of electron density, which is especially relevant for the global monitoring in real time. MIDAS (the Multi-Instrument Data Analysis System), an algorithm proposed in [24] for imaging the Earth's ionosphere, integrates various data sources to design highly accurate 3D models of ionospheric electron concentration.

Despite these achievements, there are still a number of issues related to IRT based on GNSS data that need to be addressed. The most important among them are selection of the optimal size and geometry of the reconstruction element—voxel (short for volume and pixel, a 3D equivalent of pixel), techniques for smoothing data to be reconstructed, justification of the introduced restrictions and taking into account of a priori information about the ionosphere state, as well as multidimensional optimization of the parameters of the developed algorithms [18, 25, 26]. Of particular relevance in these conditions are the methods that take into account a priori information for solution of IRT problems [10, 12].

In this paper we discuss the algorithm developed for 3D IRT and demonstrate its performance using the simulation and experimental data. The algorithm is based on the algebraic reconstruction techniques. Certain restrictions have been introduced to ensure
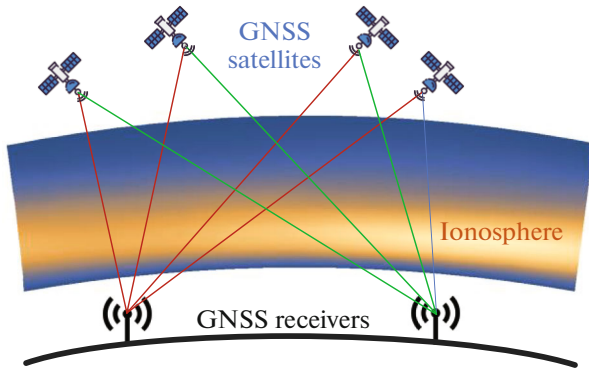
Fig. 1. The principle of IRT based on GNSS data.

stability of the problem solution. The prospects for application of the proposed approach to radio navigation systems are discussed.

The paper consists of four sections. Section 1 describes the initial data obtained during IRT with the use of GNSS signals. Section 2 presents an algorithm for 3D IRT based on algebraic reconstruction techniques taking into account a priori information. Section 3 is devoted to computer simulation of IRT techniques. Section 4 analyzes the results of the experimental verification of the 3D IRT algorithm using data from the satellite system for precise positioning (SSPP) of the Republic of Belarus. The conclusion summarizes the main results obtained in this study and outlines prospects for further research.

1. DESCRIPTION OF INITIAL DATA AND PROBLEM STATEMENT

IRT that relies on GNSS data involves image reconstruction in the region of interest by analyzing a subset of integral projections (Fig. 1). These projections correspond to the passage of radio signals along different trajectories (rays) formed by different geometries of the satellites and receiving station locations, which is equivalent to different directions (angles) of ray propagations relative to the region of interest. Inverse mathematical problems associated with image reconstruction from measurements taken along rays that either pass directly through the region of interest or bend around its periphery (around the region) are difficult to solve since the desired information, such as the electron density distribution, is not directly available [17−20]. Instead, only its certain transforms or projections are available. In practice, these measurements represent incomplete and noisy data samples [1, 9, 13, 15, 17, 27]. Ionospheric radio tomography based on satellite signals can be difficult to implement because of the limited number of satellites and ground stations, as well as the receiving aperture; also, it is required to take into account additional a priori information.

To reconstruct 3D images of the ionospheric electron density, it is necessary to calculate linear integrals based on the data obtained at different positions and orientations of ray propagation through the region observed. These linear integrals have the form of the total electron content (*TEC*), which can be written for an arbitrary time *t* as [1]

$$TEC(t) = \int_l Ne(t,l)dl, \qquad (1)$$

where $Ne(t, l)$ is the ionospheric electron density and l specifies the trajectory of signal propagation between the satellite and the receiver.

When reconstructing the ionosphere, 24 h is usually divided into time periods, each no longer than 30 min. All stages of determining the $TEC-TEC$ calculation from code and phase pseudoranges, elimination of cycle slips, and calculation of differential code biases of GNSS signals—are described in detail in the authors' previous work [13], so that in this paper, we use the results of TEC calculation obtained earlier.

In terms of computed tomography [1], and also, taking into account the fact that electron density distribution is stable over a specified period of time, the ionosphere is divided into a regular grid of *n* voxels (see Fig. 2a). This approach is based on the spatial correlation of the ionosphere, which assumes that electron density is the same within a voxel. A number of studies are devoted to the choice of voxel geometry [28, 29], as well as the use of variable-size voxels [30]. Figure 2b shows possible voxel geometry options in a rectangular coordinate system (voxel 1), in a rectangular coordinate system taking into account the curvature of the Earth (voxel 2), and in a geographic coordinate system (voxel 3).

The choice of the elementary voxel size is extremely important in IRT [18, 25, 26, 28, 29]. With a small voxel size, the spatial resolution is high, but in this case, computational costs increase and many voxels may remain unrecorded. Increasing the voxel size simplifies the reconstruction, but results in the quality loss of interpretation of the processes taking place in the ionosphere, which is unacceptable in practical applications (navigation, location, and communication). The optimal voxel size determined from the TEC measurements provides the best balance between resolution and accuracy.

Thus, during reconstruction, continuous density distribution $Ne(l)$ is discretized by column vector **x** of $n \times 1$ dimension. The set of TEC measurements is given as a column vector **y** of $m \times 1$ dimension. The linear integral in Eq. (1) includes the slant contribution of TEC along the entire trajectory of the ray from the satellite to the receiver. The parametric representation of Eq. (1) may be written as follows:

$$TEC = \sum_{i=1}^{n} a_i Ne(r,t) + \varepsilon, \qquad (2)$$

where i and a are the sampling point and the weight for numerical integration over the sampling points, respectively; n is the total number of voxels in the ionospheric grid; ε is the measurement and simulation error.

The set of all m measurements (2) can be represented as a discrete mathematical problem. With this purpose, we introduce matrix **A** that relates the electron density distributions to the *TEC* measurements. Then expression (2) can be written as

$$\mathbf{y} = \mathbf{Ax} + \boldsymbol{\varepsilon}, \tag{3}$$

where **A** is an $m \times n$ matrix that relates the electron density distributions to the *TEC* measurements; $\boldsymbol{\varepsilon}$ is an $m \times 1$ column vector of observation noise.

In this case, the IRT problem is reduced to the calculation of the unknown distribution of electron density **x** in a specified observation region using the known *TEC* measurement values of **y** and coefficient matrix **A**.

2. ALGORITHM FOR 3D IONOSPHERIC RADIO TOMOGRAPHY

Many various reconstruction algorithms have been proposed to solve the IRT problem in recent years [1, 17−20, 25, 26]. Of these, the most widely used are iterative techniques, which can be grouped into two categories [25, 26]:

• iterative algebraic reconstruction technique (ART), the Kaczmarz method, or classical ART; randomized and symmetric Kaczmarz methods;

• iterative simultaneous algebraic reconstruction technique (SART)—the classical SART algorithm, the component averaging method (CAV), the Cimmino, Landweber and diagonally relaxed orthogonal projections (DROP) methods.

The main drawback of ART algorithms is their high sensitivity to initial approximation and high computational costs. Such techniques allow good reconstruction of high-contrast (very distinct against the surrounding background) image details, which, however, may be lacking in the initial approximations in IRT. At the same time, reconstruction of the general background is performed less accurately and more slowly and is often accompanied by the occurrence of artifacts in the form of "waves" and "beats" in the background areas of the reconstructed image. In such cases, it makes sense to proceed to more complicated SART algorithms with regularization, which take proper account of a priori information, and as a result, they deal with the above problems more effectively.

Iterative SARTs are used in cases where the available measurements or observations are incomplete, noisy or have constraints [18]. SARTs allow finding the optimal solution to the inverse reconstruction problem since they take into account all available data and constraints and, thus, make it possible to obtain
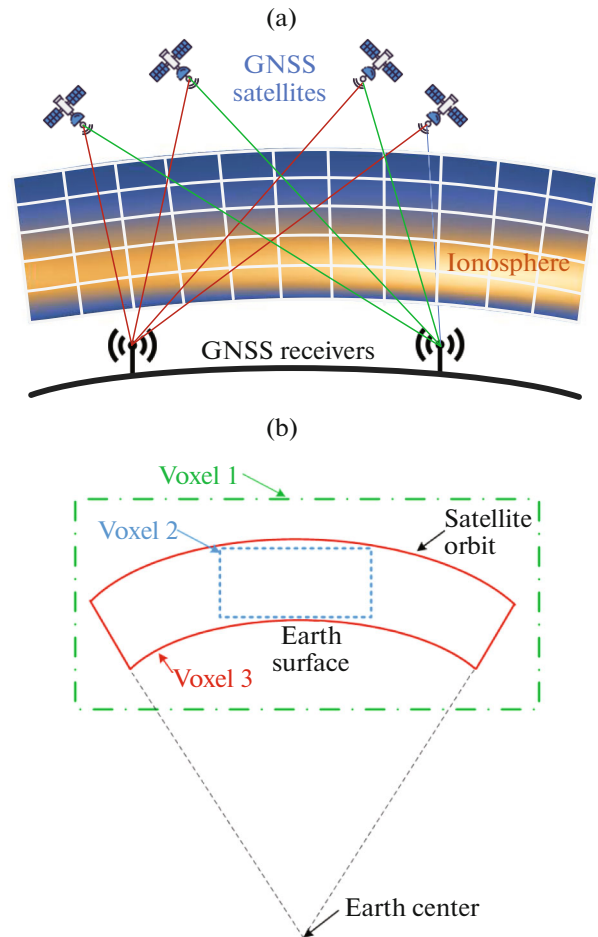
Fig. 2. Discretization of the ionosphere: (a) 3D voxels of the ionosphere; (b) approaches to choosing the geometry of one voxel.

more accurate and high-quality estimates in comparison with classical ART algorithms, which can be useful for understanding ionospheric processes and predicting ionospheric activity.

However, when determining the initial values for SART, it is also necessary to use empirical ionospheric models that reflect only the average monthly variation of the ionosphere, which is why the accuracy of the tomographic results is low. These shortcomings are eliminated using the constrained algebraic reconstruction technique (CART) [25, 26].

During the research, we carried out a comparative analysis of reconstruction algorithms, which showed that it is advisable to design the algorithm being developed for reconstructing the ionosphere with constraints on the basis of the Landweber method [18, 25], which is characterized by the lowest computational complexity and high convergence rate. The Landweber algorithm is based on an iterative procedure for minimizing the mismatch functional by sequentially updating the solution in the direction of the antigradient. At each step, the current estimate is

Table 1. Comparison of 3D reconstruction methods

Reconstruction method	Runtime	Number of iterations	Normalized residual by measurements $\mathbf{y}$	Normalized residual by image $\mathbf{x}$
Iterative algebraic reconstruction technique (ART)				
Kaczmarz method	248.14 s	458	0.357	0.684
Randomized and symmetric Kaczmarz methods	684.1 s	587	0.116	0.783
Symmetric Kaczmarz method	212.98 s	172	0.127	0.846
Iterative simultaneous algebraic reconstruction techniques (SART)				
Classical SART	0.48 s	1483	0.109	0.992
Landweber method	0.23 s	584	0.249	0.956
Cimmino method	0.368 s	746	0.277	0.908
CAV	0.288 s	897	0.288	0.892
DROP	0.562 s	751	0.281	0.921

refined, taking into account the difference between the calculated and measured data, the weighted matrix of the forward problem operator, which ensures stable convergence of the algorithm with low computational complexity.

The comparative analysis, the results of which are presented in the table, has confirmed that the Landweber algorithm is most suitable for the 3D reconstruction method being developed, since it demonstrates one of the best ratios between the computational efficiency (runtime—0.23 s) and accuracy (measurement residual—0.249, image residual—0.956).

This is also true for Kaczmarz methods; compared to them, the Landweber algorithm provides higher accuracy with comparable runtime. Although the algorithms, such as DROP and CAV, have similar computational efficiency, they require more iterations and show worse results.

All algorithms were tested on the same computing equipment: AMD Ryzen 7 7700 processor (8 cores, 3.8 GHz) with 32 GB of DDR4 RAM. The algorithms were implemented in the MATLAB environment with built-in functions to work with matrices. The calculation was performed on an 8-core processor. The time values (see Table 1) are the average for 10 independent runs for each algorithm on the same data set with a size of 14850 (the number of voxels by latitude is 18, 33—by longitude, and 25 by height). It should be noted that although the program execution time is specific to each particular computing platform and implementation, the relative ratios of the algorithm execution speed allow us to compare them in terms of their computational efficiency. On other platforms, though the absolute time values may differ, but the ratio between the algorithms will remain the same.

The results shown in Table 1 were obtained in the simulation aimed to estimate the efficiency of differ-

ent reconstruction algorithms. The simulation conditions, including noise parameters, the model used, and the experimental methodology, are described in detail in Section 3.

To take into account the constraints on the smoothness of the electron density distribution, we introduced $n \times n$ matrix $\mathbf{B}$, which links adjacent voxels using a 9-point finite-difference approximation of the Laplace operator [25, 26]. For this purpose, the observation Eq. (3) is supplemented with the following:

$$\alpha \mathbf{B}\mathbf{x} + \boldsymbol{\varepsilon}_{sm} = 0, \tag{4}$$

where $\boldsymbol{\varepsilon}_{sm}$ is the approximation noise; α is the weighting coefficient at which the approximation noise and the noise ε are equal in level.

The developed algorithm was modified for the initial data and it is reduced to an iterative calculation of the expression

$$\hat{\mathbf{x}}^{k+1} = \hat{\mathbf{x}}^{k} + \beta\lambda_k \tilde{\mathbf{A}}^{\mathrm{T}}\left(\tilde{\mathbf{y}} - \tilde{\mathbf{A}}\hat{\mathbf{x}}^{k}\right), \tag{5}$$

where $\hat{\mathbf{x}}^{k}$ is the estimate of the electron concentration vector $\mathbf{x}$ at the nodes of the $m \times n$ grid at the k-th iteration; β is the coefficient taking into account the weight of the a priori values of vector $\hat{\mathbf{x}}^{0}$; λ_k is the relaxation coefficient that takes into account the a priori distribution of the electron concentration; $\tilde{\mathbf{A}} = \left\|\mathbf{A} \ \mathbf{B}\right\|^{\mathrm{T}}$ is the augmented observation matrix supplemented with the constraint matrix $\mathbf{B}$; $\tilde{\mathbf{y}} = \left\|\mathbf{y} \ \mathbf{O}\right\|^{\mathrm{T}}$ is the augmented observation vector supplemented with the zero n-dimensional vector $\mathbf{O}$.

The algorithm proposed for 3D reconstruction of the ionosphere based on the modified Landweber algorithm with the introduced constraints consists of the following stages [27]:

• determination of spatial resolution;

• reception of incoming input measurements y;

• calculation of matrix **A** components based on data on the coordinates of satellites and ground stations;

• setting of the initial values of $\mathbf{x}^0$ taking into account the data of the IRI-2016 ionospheric model [31−33] or the constraints according to Chapman [1] in the absence of a priori information;

• initialization of λ_k with the data on the a priori distribution of electron concentration [31−33];

• calculation of the constraint matrix **B** [25, 26] and its addition to matrix **A**;

• calculation of expression (4) until the required accuracy is achieved (decision to stop the iterations).

The vector of measurements **y** (with $m \times 1$ dimensions), which contains the values of the *TEC* in the ionosphere along the lines of "satellite − ground receiving station" (1)−(3), arrives at the input of the reconstruction algorithm. The spatial resolution is determined by the number of voxels in height n_h, latitude n_{lat} and longitude n_{lon}. The total dimension n of the vector x being reconstructed is given as

$$n = n_h \times n_{lat} \times n_{lon}.$$

While calculating the observation matrix **A** for each ray (satellite − ground station), we determine the voxels intersected by this ray. The length of the ray intersection with each of such voxels is recorded in the corresponding matrix cell; the elements corresponding to the voxels through which the ray does not pass are equal to zero.

An example of the calculated observation matrix is shown in Fig. 3 for the following initial data: the total number of voxels is 108 000 (number of voxels: 60 in latitude, 60 in longitude, and 30 in height); the total number of *TEC* measurements is 564 (for 94 stations and 6 satellites for each station).

To determine the initial state of the electron density in the nodes of the voxel grid $\mathbf{x}^0$, we use both the empirical data from the model of International Reference Ionosphere (IRI) 2016 [31−33] and analytical approaches. IRI-2016 provides information on the height levels and seasonal variations of the ionosphere for different geographic coordinates. The Chapman profile (for night-time) and the exponential model (for day-time) are used at the modeling stage.

It is advisable to calculate the initial value of vector $\mathbf{x}^0$ being reconstructed for night-time, as well as the relaxation coefficient λ_k in accordance with the Chapman equation, which describes the distribution of electrons in the ionosphere Ne_{Chap} depending on the height [14]:

$$Ne_{Chap}(h_r) = Ne_{max} \exp\left(c\left[1 - h_r - \exp(-h_r)\right]\right), \quad (6)$$

where Ne_{max} is the maximum value of the electron density (at the ionospheric pierce point (IPP) height; c is the index of the Chapman equation (at $c = 0.5$, the
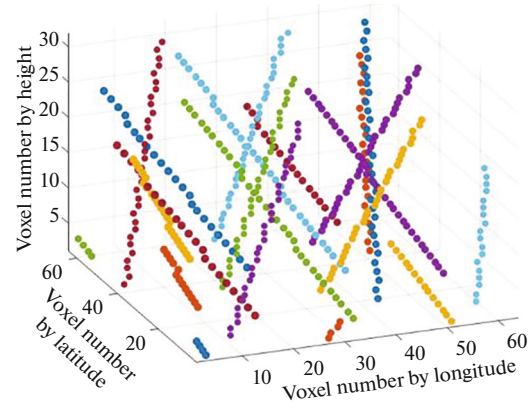

Fig. 3. Example of the calculated observation matrix **A**.

equation is called α-Chapman; at $c = 1$, β-Chapman); h_r is the reduced height.

Day-time conditions are better represented by the exponential distribution Ne_{exp} [14]:

$$Ne_{exp}(h_r) = Ne_{max} \exp(-h_r). \quad (7)$$

Figure 4 illustrates the calculation of a two-dimensional a priori spatial distribution of the electron concentration in accordance with Eqs. (6), (7).

The Chapman equation and the exponential function are based on the physics of the atmosphere and the results of its long-term observation, so that they allow taking into account a priori information on the distribution of electrons in the ionosphere by height at the stage of its reconstruction. It is assumed that the ionosphere consists of a single layer of electrons that are exponentially distributed by height. In Eqs. (6), (7), an assumption is introduced that there are no oscillations in the ionosphere in the horizontal plane, and the absorption coefficient of solar radiation is constant (which is equivalent to the assumption of monochromatic radiation).

Although the real state of the ionosphere may be more complex, Eqs. (6), (7) allow us to quickly process the observations and present the a priori distribution of the ionosphere by height for its subsequent reconstruction. Coefficient β in (4) makes it possible to take into account the weight of the a priori value of $\mathbf{x}^0$ obtained in accordance with Eqs. (6)−(7) taking into account the averaged values of **y** over the entire set of voxels.

As can be seen in Fig. 5a, some voxels (for example, x_5) are not covered by observations, i.e. the model under consideration does not provide complete coverage. In the frames of the standard reconstruction procedure, the values of such voxels will converge to the a priori specified ones. To eliminate this discrepancy, we introduce matrix **B**, which imposes constraints on the smoothness of the distribution function. Then, if not a single ray passes through a voxel, the latter will
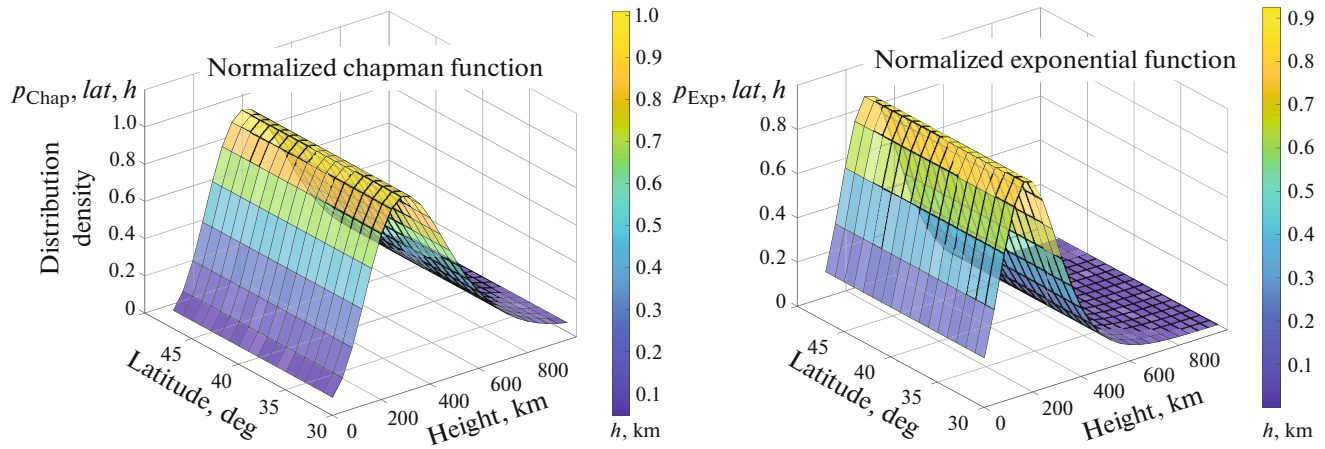
Fig. 4. Examples of the calculation of the a priori spatial distribution of electrons in the ionosphere.
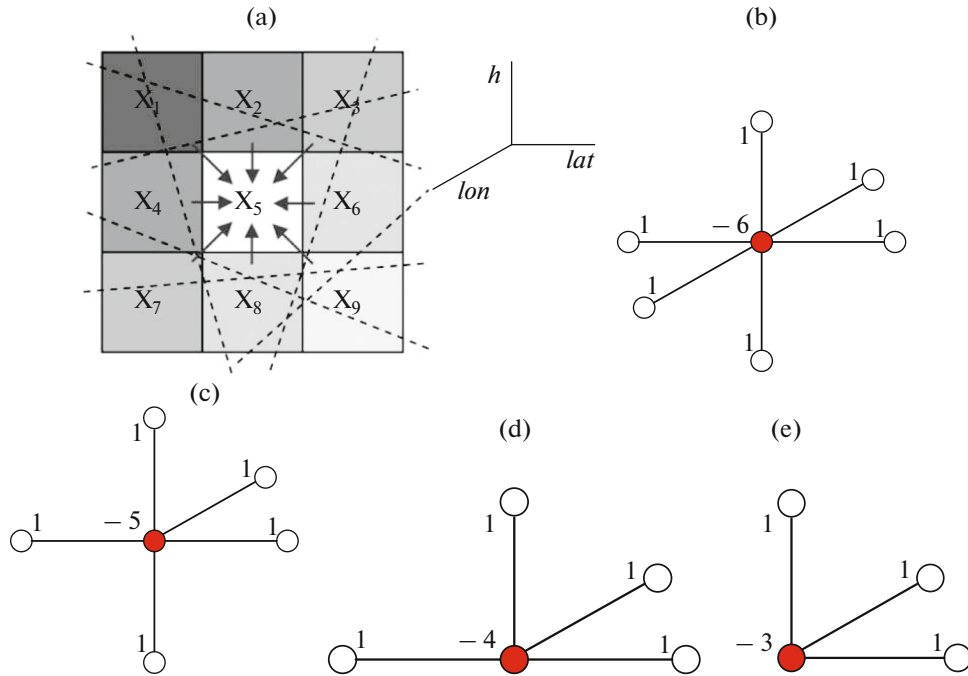

Fig. 5. Schematic of a constraint matrix construction based on the second-order Laplace operator: (a) two-dimensional plane; (b) central element; (c) face; (d) edge; and (e) vertex.

extract information from its neighbors, and a voxel that has a sufficient number of independent measurements at its disposal (overdetermined) takes its value as a result of direct calculation from the initial data. In order to ensure the smoothness of the solution and the influence of local features on adjacent areas, equations relating the values of adjacent voxels are added to the final system.

In particular, the differences between the value of the current voxel and the average over its nearest neighbors are included in the regularization functional (or matrix **B**), the minimization of which contributes

to smoothing. This procedure is mathematically written as an additional system of linear equations (4).

The correct choice of matrix **B** in (8) plays a crucial role in the reconstruction of the electron density distribution in the ionosphere. One way to solve this problem is to use a multipoint finite-difference approximation of the second-order Laplace operator [25, 26]. The main idea of this approach for the two-dimensional case is illustrated in Fig. 5a. The cells x_j ($j = 1, 2, ..., 9$) are shaded in gray in an arbitrary scale. The measuring ray never intersects the cell in the center (x_5). Imposing a constraint in the form of a
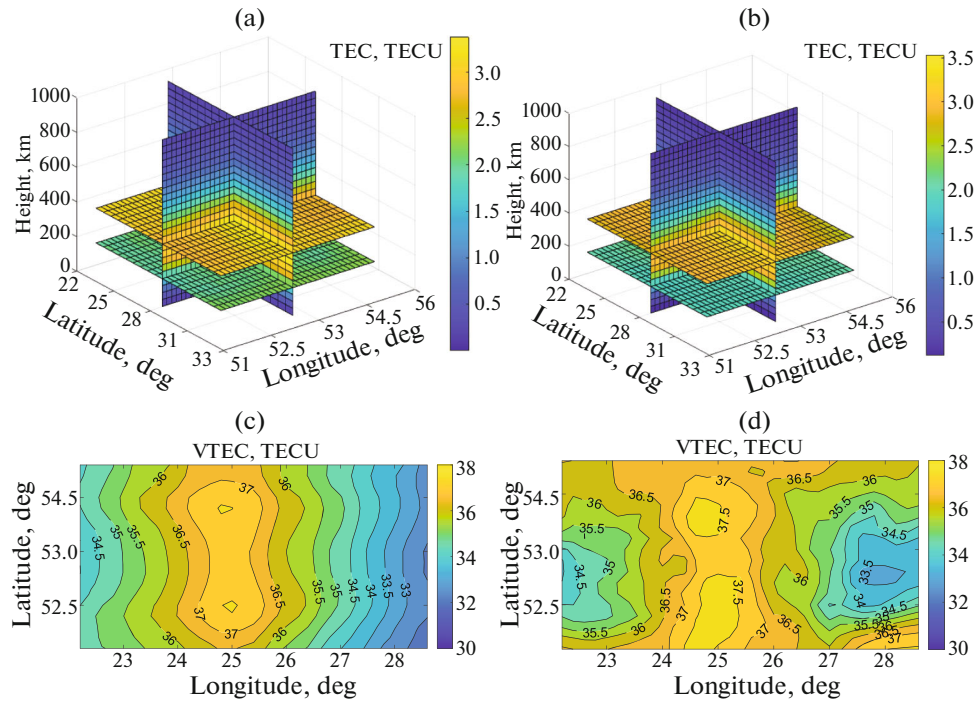
Fig. 6. Mathematical model of the ionosphere and the results of its reconstruction: (a) sections by height and latitude and (c) *VTEC*; (b) sections by height and latitude, and (d) *VTEC*.

Laplacian on the base field allows us to derive the value of $\mathbf{x}_5$ from the adjacent cells.

In accordance with the basic rules, the constraints for voxels lying in the center of the observed area are specified using a nine-point finite-difference approximation of the second-order Laplace operator shown in Fig. 5b (the voxel being reconstructed is shown in red). When voxels are located on the boundary of the observed area, the operator must be adjusted accordingly. The rules for voxels located on the face (Fig. 5c), edge (Fig. 5d) and vertex (Fig. 5e) are formed individually. For the remaining layers, operators are specified according to the previous rules. Note that other approaches to the formation of discrete Laplacians in the reconstruction of 3D images also allow us, to a certain degree or adaptively, to take into account the correlation of the values of adjacent voxels [34−36].

It is important that the regularization matrix **B** is calculated once before the iteration process starts and it remains constant at all steps of the algorithm. Each element of matrix **B** is a weight coefficient corresponding to the pattern of the nine-point Laplace operator, as shown in Fig. 5.

Since matrix **A** is supplemented with an $n \times n$-dimensional constraint matrix **B**, the input vector **y** is supplemented with a vector of zero values of $n \times 1$ dimension in order to maintain the dimensions.

3. RESULTS OF COMPUTER SIMULATION

To study the performance of the reconstruction algorithm, we carried out the mathematical simulation using the following initial data: the total number of voxels was 14850 (the number of voxels: 18—in latitude, 33—in longitude, and 25—in height); the total number of *TEC* measurements was 564 (for 94 stations and 6 satellites for each station). Let us represent the voxels in the geodetic coordinate system (Figs. 6a, 6b). The controlled parameters are the discrepancies in measurements and images.

Figure 6 shows the initial mathematical model of the ionosphere and the results of its reconstruction based on artificial noise data in the form of the distribution of the vertical total electron content (*VTEC, TECU*) in various sections—in latitude, longitude, and height. In the framework of the simulation, noisy measurements were formed as follows: an additive normally distributed random error was added to the vector of real *TEC* values. The noise level was 1% of the average value of the measurement vector, which allowed us to reproduce the random measurement noise that occurs in real conditions as a result of ambiguities in phase measurements and instrument errors.

In the practical implementation of ionospheric reconstruction algorithms, of critical importance is the choice of weighting coefficients α (considering smoothness constraints) and β (considering a priori values). This procedure is nontrivial and requires the use of parametric optimization methods.
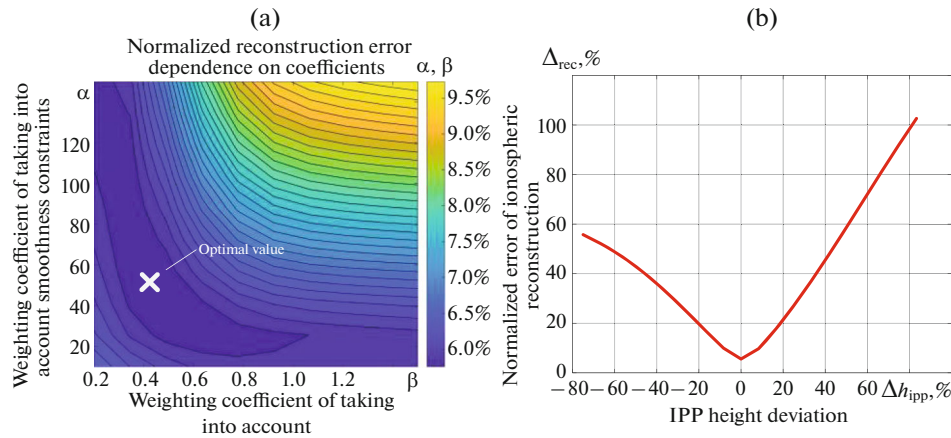
Fig. 7. Dependence of the reconstruction quality on (a) the choice of weighting coefficients α, β and (b) the IPP height.

During the analysis of the reconstruction results using model data, we determined the optimal values of the weighting coefficients: $\alpha = 50$ to take into account smoothness constraints and $\beta = 0.4$ to take into account a priori information (see Fig. 7a).

When using the a priori values given by Eqs. (4)–(7) and also, when calculating *VTEC*, the key factor is determination of the IPP height, where the maximum electron density is observed. This height varies depending on the region, time of day, and season. For example, according to the IRI-2016 with the IGRF-13 coefficients for 2020, in the Minsk region, the IPP height varied from 220 to 350 km [32]. Figure 7b shows the dependence of the percentage reconstruction error on the deviation in the choice of the IPP height. It is evident from the graph that the reconstruction error is minimal if the IPP height coincides with its true value, and it increases linearly with the discrepancy between the true IPP height and the height used in the reconstruction algorithm. A 20% error in determining the IPP height causes an increase in the normalized reconstruction error of up to 20%.

4. RESULTS OF THE EXPERIMENTAL STUDIES

To demonstrate the performance of the proposed algorithm, we conducted experimental studies using the data for February 27, 2023, which was a period of a strong geomagnetic storm with the $K_p = 7$, with the aurora polaris observed over the territory of the Republic of Belarus. The source information was RINEX files (navigation and observation data) from the SSPP. The 3D reconstruction was carried out based on the results of the TEC measurements for 94 SSPP stations. A 15-min sampling rate was chosen to ensure the required amount of data. The IRI-2016 data were used as initial conditions.

Figure 8 shows the TEC calculated using the methodology proposed in [13]. The graph in Fig. 8a shows the TEC variations for the SSPP Rechitsa station; the TEC obtained for different GNSS satellites are shown in different colors. The graph clearly shows the characteristic daily variations and fairly large fluctuations associated with the geomagnetic storm. The graph in Fig. 9b displays the averaged TEC values for all 94 observation stations, which makes it possible to show the general dynamics of ionospheric disturbances over the region on February 27, 2023.

Figure 9 shows the calculation results for the *VTEC* spatial distribution over the territory of Belarus and adjacent countries at different points in time: 08:00 UTC—the initial phase of the disturbance; 10:00 UTC—the development of the ionospheric storm; 12:00 UTC—the maximum phase of the disturbance, 14:00 UTC—the recovery phase. The maps clearly demonstrate the significant spatial heterogeneity of the electron distribution, characteristic of periods of geomagnetic disturbances.

Figure 10 shows a 3D reconstruction of the electron concentration fields in the ionosphere performed using the proposed algorithm based on the data from 94 SSPP ground stations and 6 satellites per station during the geomagnetic storm on February 27, 2023 over the territory of Belarus. The total number of voxels *n* was 14 850 (18, 33, and 25 in latitude, longitude, and height, respectively). Also shown are the sections of the reconstructed region in two planes (with a constant latitude of 54° and a constant longitude of 27.5°) and the *VTEC* obtained by the summation of the reconstructed field over vertical columns.

In addition, Fig. 10 clearly shows the characteristic maximum of the electron concentration at heights of 300–400 km, which corresponds to theoretical ideas about the ionospheric structure. Of particular interest are significant horizontal inhomogeneities in the *VTEC* distribution, which are typical for periods of geomagnetic disturbances. The results obtained demonstrate a high degree of consistency between the reconstructed and physical models of the ionosphere.
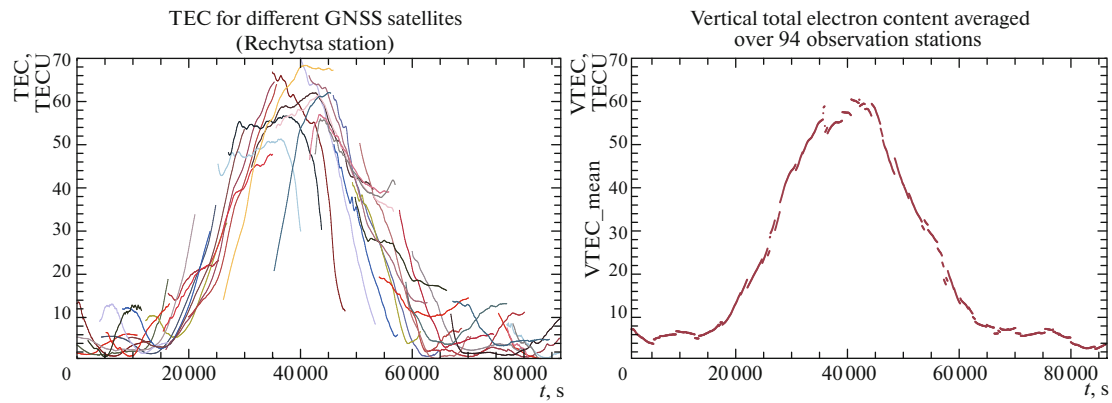
Fig. 8. *VTEC* time dependence over the territory of the Republic of Belarus on February 27, 2023: (a) according to the data from one Rechytsa station and (b) averaged over 94 stations.
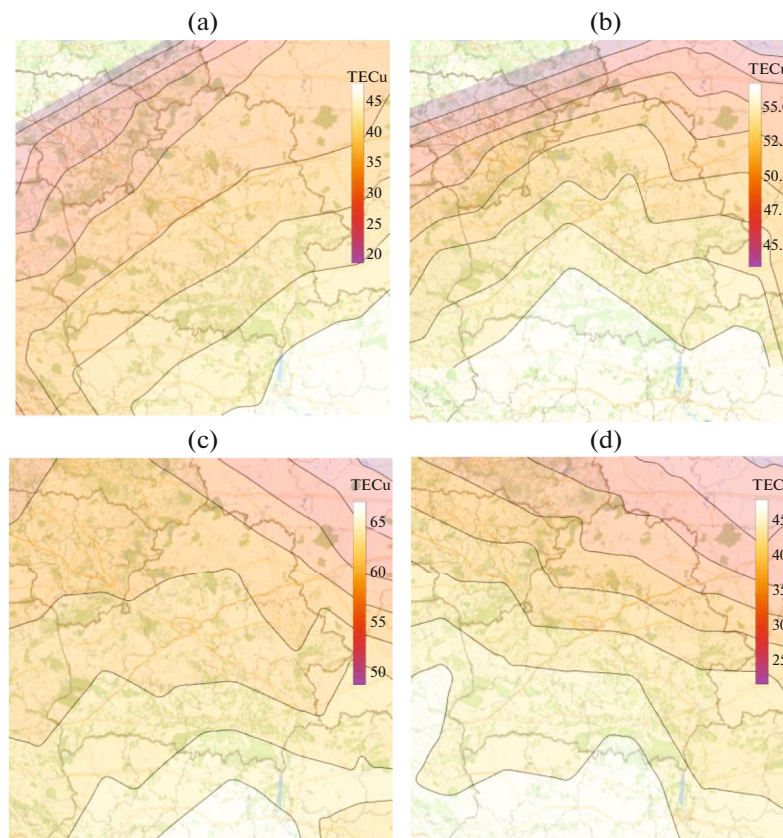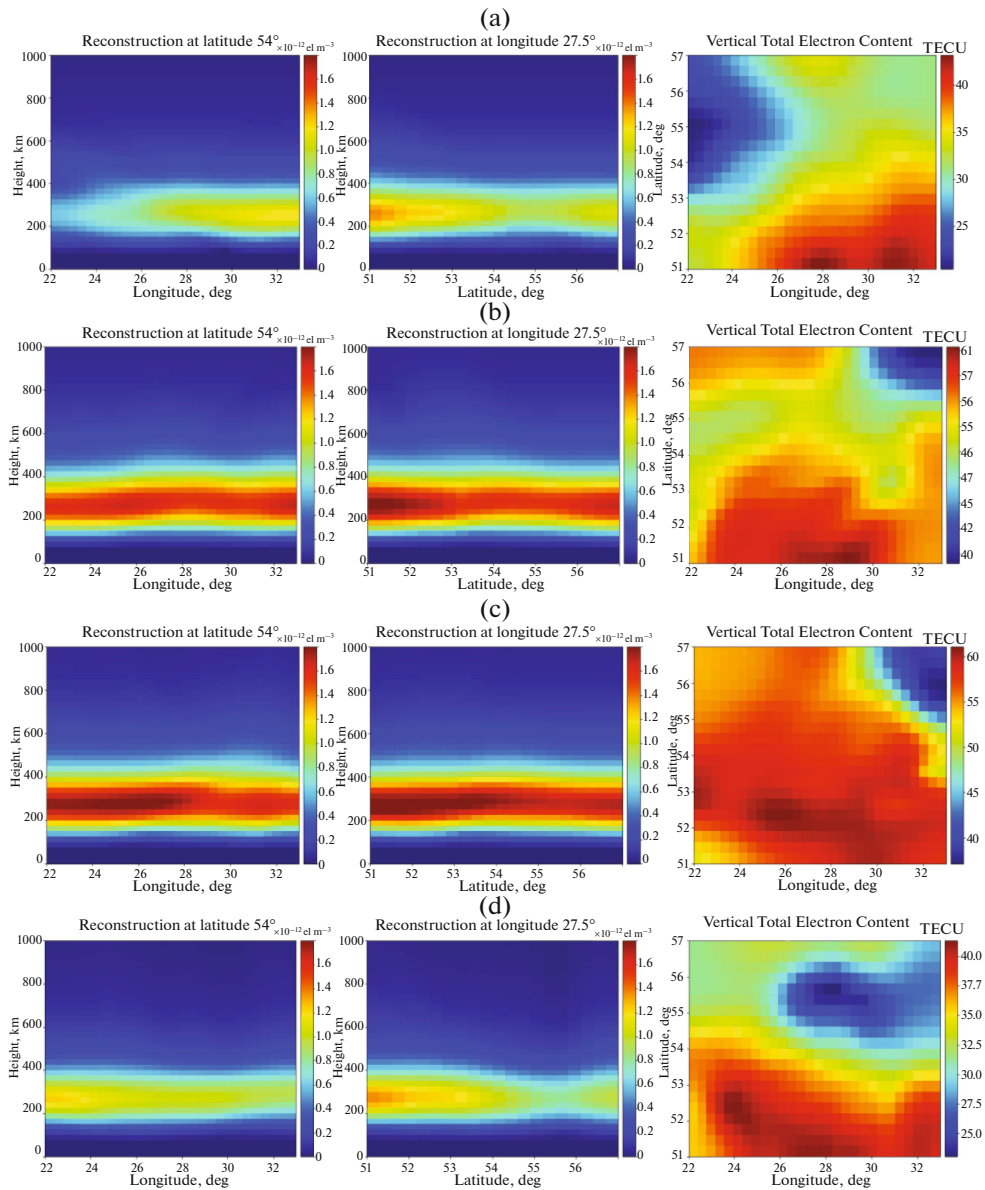

Fig. 9. An example of *VTEC* interpolation at different points in time on February 27, 2023, based on data from GNSS satellites and 94 observation stations over the territory of the Republic of Belarus and adjacent states: (a) 08:00:00; (b) 10:00:00; (c) 12:00:00; (d) 14:00:00.

They allow detailed observation and analysis of the dynamics of ionospheric disturbances during a geomagnetic storm. Experimental verification of the algorithm using real data has confirmed its effectiveness and practical applicability to the monitoring of the ionosphere state the under conditions of geomagnetic disturbances.

CONCLUSIONS

The article presents a comprehensive approach to the problem solution of 3D IRT of the electron concentration in the ionosphere using GNSS data. The following main results have been obtained in this study:

Fig. 10. An example of reconstruction of the electron distribution at different points in time on February 27, 2023, based on data from GNSS satellites and 94 SSPP observation stations over the territory of the Republic of Belarus and adjacent states: (a) 08:00:00; (b)10:00:00; (c)12:00:00; (d)14:00:00.

(1) a modified algorithm for simultaneous algebraic reconstruction with introduced constraints based on the Landweber method has been developed and implemented. The algorithm is characterized by a high convergence rate and relatively low computational complexity, which makes it promising for use in real-time systems;

(2) mathematical simulation was performed to estimate the efficiency of the algorithm with the following parameters: 14 850 voxels (18 in latitude, 33 in longitude, and 25 in altitude) and 564 *TEC* measurements (for 94 stations and 6 satellites for each station). The simulation results have confirmed the algorithm

robustness to measurement noise and the ability to reconstruct the spatial structure of ionospheric homogeneities;

(3) optimal weighting coefficients of the algorithm have been determined to take into account a priori information ($\beta = 0.4$) and smoothness constraints ($\alpha = 50$), ensuring stable reconstruction with a sampling rate of 15 min, as well as a balance between it and spatial resolution;

(4) the algorithm was experimentally verified on real data from RINEX files of the satellite system of precise positioning of the Republic of Belarus for Feb-

ruary 27, 2023, during a strong geomagnetic storm ($K_p = 7$).

The results obtained have demonstrated the ability of the algorithm to effectively reconstruct the 3D structure of the ionosphere even under conditions of significant disturbances and can be used to develop systems for real-time monitoring of the ionosphere state. The proposed algorithm can be used in various applications, such as space weather forecasting, ensuring reliable operation of satellite navigation and communication systems, as well as in fundamental studies of ionospheric processes.

Promising areas of further scientific research are the development of methods for integrating data from different sources, including ionosondes, to improve the accuracy of reconstruction; optimization of IRT algorithm parameters; accounting for geodetic and temporal variations in the distribution of electrons; analysis under conditions of extreme geomagnetic disturbances, as well as development of systems for real-time monitoring of the ionosphere state for space weather forecasting and ensuring stability of radio engineering systems.

CONFLICT OF INTEREST

The authors of this work declare that they have no conflicts of interest.

REFERENCES

1. Kunitsyn, V.E., Tereshchenko, E.D., and Andreeva, E.S. *Radiotomografiya ionosfery* (Tomography of the Ionosphere), Moscow: Fizmatlit, 2007.

2. Afraimovich, E.L., Astafyeva, E.I., Demyanov, et al., A review of GPS/GLONASS studies of the ionospheric response to natural and anthropogenic processes and phenomena, *Space Weather Space Clim.*, 2013, vol. 3. https://doi.org/10.1051/swsc/2013049.

3. Hofmann-Wellenhof, B., Lichtenegger, H., and Wasle, E., *GNSS − Global Navigation Satellite Systems. GPS, GLONASS, Galileo, and More*, Springer, 2008.

4. Solonar, A.S., Khmarski, P.A., and Tsuprik, S.V., Tracking estimator of the ground target coordinates and motion parameters using onboard optical location system data, *Gyroscopy and Navigation*, 2023, vol. 14, no. 3, pp. 244−258. https://doi.org/10.1134/S2075108723030082

5. Solonar, A.S., Khmarski, P.A., Naumov, A.O., et al., The use of numerical Monte Carlo integration to verify the physical feasibility of a trajectory based on surveillance radar data, *Stochastic Modelling and Computational Sciences*, 2023, vol. 3, no. 1, pp. 59−73. https://doi.org/10.61485/smcs.27523829/v3n1p5

6. Solonar, A.S. and Khmarski, P.A., Main problems of trajectory processing and approaches to their solution within the framework of multitarget tracking, *J. Phys. Conf. Ser.*, 2021, vol. 1864. https://doi.org/10.1088/1742-6596/1864/1/012004

7. Yasyukevich, Y.V., Zhang, B., and Devanaboyina, V.R., Advances in GNSS positioning and GNSS remote sensing, *Sensors*, 2024, vol. 24, no. 4, pp. 1200. https://doi.org/10.3390/s24041200

8. Astafyeva, E., Yasyukevich, Y., Maksikov, A., and Zhivetiev, I., Geomagnetic storms, super-storms, and their impacts on GPS-based navigation systems, *Space Weather*, 2014, vol. 12, pp. 508−525. https://doi.org/10.1002/2014SW001072

9. Yasyukevich, Yu.V., Mylnikova, A.A., and Polyakova, A.S., Estimating the total electron content absolute value from the GPS/GLONASS data, *Results in Physics*, 2015, vol. 5, pp. 32−33. https://doi.org/10.1016/j.rinp.2014.12.006

10. Nesterov, I.A. and Kunitsyn, V.E., GNSS radio tomography of the ionosphere: The problem with essentially incomplete data, *Advances in Space Research*, 2011, vol. 47, issue 10, pp. 1789−1803. https://doi.org/10.1016/j.asr.2010.11.034

11. Kunitsyn, V.E., Nesterov, I.A., Padokhin, A.M., et al., Ionospheric radio tomography based on the GPS/GLONASS navigation systems, *Journal of Communications Technology and Electronics*, 2011, vol. 56, pp. 1269−1281. https://doi.org/10.1134/S1064226911100147

12. Kunitsyn, V.E., Andreeva, E., Nesterov, I.A., Padokhin, A.M., Ionospheric sounding and tomography by GNSS, *Geodetic Sciences − Observations, Modeling and Applications*, 2013. https://doi.org/doi: https://doi.org/10.5772/54589.

13. Naumov, A.O., Khmarskiy, P.A., Byshnev, N.I., and Piatrouski, M.A., Determination of total electron content in the ionosphere over the territory of the Republic of Belarus based on global navigation satellite systems data, *Vestsi Natsyyanal'nai akademii navuk Belarusi. Seryya fizika-technichnykh navuk* (Proceedings of the National Academy of Sciences of Belarus. Physical-technical series), 2024, vol. 69, no. 1, pp. 53−64. https://doi.org/10.29235/1561-8358-2024-69-1-53-64.

14. Stankov, S.M., Stegen, K., Muhtarov, P., and Warnant, R., Local ionospheric electron density profile reconstruction in real time from simultaneous ground-based GNSS and ionosonde measurements, *Advances in Space Research*, 2011, vol. 47, issue 7, pp. 1172−1180. https://doi.org/10.1016/j.asr.2010.11.039

15. Naumov, A.O., Khmarski, P.A., Aronov, G.A., and Kotov, D.S., Results of studies on processes occurring in the ionosphere and Earth's magnetic field over the territory of the Republic of Belarus for the year 2023, *Nonlinear Phenomena in Complex Systems*, 2024,

vol. 27, no. 3, pp. 225−233.
https://doi.org/10.5281/zenodo.13960570

16. Chen, C., Pavlov, I., Padokhin, A., Yasyukevich, et al., Galileo and BeiDou AltBOC Signals and Their Perspectives for Ionospheric TEC Studies, *Sensors*, 2024, vol. 24, no. 6472.
https://doi.org/10.3390/s24196472

17. Artemiev, V.M., Naumov, A.O., Stepanov, V.L., and Murashko, N.I., Method and results of real time modeling of ionosphere radiotomography on the basis of the Kalman filter theory, *Journal of Automation and Information Sciences*, 2008, vol. 40, no. 2, pp. 52−62.
https://doi.org/10.1615/JAutomatInfScien.v40.i2.50

18. Herman, G.T., *Fundamentals of Computerized Tomography, Image Reconstruction from Projections*, Springer, New York, 2009.

19. Zolotarev, S.A., Ahmed Talat Taufik Taruat, and Bilenko, E.G., Taking into account a priori information in the iterative reconstruction of images of foundry products, *Vestsi Natsyyanal'nai akademii navuk Belarusi. Seryya fizika-technichnykhnavuk* (Proceedings of the National Academy of Sciences of Belarus. Physical-technical series), 2023, vol. 68, no. 3, pp. 242−251.
https://doi.org/10.29235/1561-8358-2023-68-3-242-251.

20. Zolotarev, S.A., Vengrinovich, V.L., and Smagin, S.I., Iterative tomography of pipes during operation, *Vestsi Natsyyanal'nai akademii navuk Belarusi. Seryya fizika-technichnykh navuk*, 2021, vol. 66, no. 4, pp. 505−512.
https://doi.org/10.29235/1561-8358-2021-66-4-505-512

21. Bust, G.S., Garner, T.W., and Gaussiran, T.L., II Ionospheric Data Assimilation Three-Dimensional (IDA3D): A global, multisensor, electron density specification algorithm, *Journal of Geophysical Research*, 2004, vol. 109, A11.
https://doi.org/10.1029/2003JA010234

22. Bruno, J., Mitchell, C.N., Bolmgren, K.H.A., Witvliet, B.A., A realistic simulation framework to evaluate ionospheric tomography, *Advances in Space Research*, 2020, vol. 65, issue 3, pp. 891−901.
https://doi.org/10.1016/j.asr.2019.11.015

23. Bust, G.S. and Mitchell, C.N., History, current state, and future directions of ionospheric imaging, *Reviews of Geophysics*, 2008, vol. 46, RG1003.
https://doi.org/10.1029/2006RG000212

24. Mitchell, C.N. and Cannon, P.S., Multi-Instrument Data Analysis System (MIDAS) Imaging of the Ionosphere, *Advances in Space Research*, 2002, pp. 147−152.

25. Hobiger, T., Kondo, T., and Koyama, Y., Constrained simultaneous algebraic reconstruction technique (C-SART) − a new and simple algorithm applied to ionospheric tomography, *Earth Planet.*, 2008, vol. 60, pp. 727−735.
https://doi.org/10.1186/BF03352821

26. Wen, D., Liu, S., and Tang, P., Tomographic reconstruction of ionospheric electron density based on constrained algebraic reconstruction technique, *GPS Solution*, 2010, vol. 14, pp. 375−380.
https://doi.org/10.1007/s10291-010-0161-0

27. Khmarski, P.A. and Naumov, A.O., Algorithms for three-dimensional reconstruction of electron concentration fields in the ionosphere using data from the global navigation satellite system, *Proceedings 31st Saint Petersburg International Conference*, Saint-Petersburg, 2024, pp. 185−188.

28. Lu, W., Ma, G., and Wan, Q., A review of voxel-based computerized ionospheric tomography with GNSS ground receivers, *Remote Sensing*, 2021, vol. 13, no. 3432.
https://doi.org/10.3390/rs13173432

29. Sutton, E. and Na, H., Comparison of geometries for ionospheric tomography, *Radio Sci.*, 1995, vol. 30, pp. 115−125.

30. Semeter, J. and Kamalabadi, F., A natural pixel decomposition for tomographic imaging of the ionosphere, *In Proceedings of the 1998 IEEE International Conference on Acoustics, Speech and Signal Processing*, Seattle, 1998, vol. 5, pp. 2913−2916.

31. Yasyukevich, Y.V., Zatolokin, D., Padokhin, A., et al., Klobuchar, NeQuickG, BDGIM, GLONASS, IRI-2016, IRI-2012, IRI-Plas, NeQuick2, and GEMTEC ionospheric models: A comparison in total electron content and positioning domains, *Sensors*, 2023, vol. 23, no. 10, p. 4773.
https://doi.org/10.3390/s23104773

32. International Reference Ionosphere. https://ccmc.gsfc.nasa.gov/modelweb/models/iri2016_vitmo.php (Accessed June 7, 2023).

33. Ivanov, V.B., Zatolokin, D.A. & Gorbachev, O.A. Comparing models of total electron content in the ionosphere for GLONASS. *Gyroscopy Navig.* 8, 295−299 (2017).
https://doi.org/10.1134/S2075108717040071

34. Dehghan, Mehdi & Mohebbi, Akbar, 2008. High-order compact boundary value method for the solution of unsteady convection−diffusion problems, *Mathematics and Computers in Simulation (MATCOM)*, Elsevier, vol. 79(3), pp. 683−699.
https://doi.org/10.1016/j.matcom.2008.04.015

35. Spotz, W.F., *High-order compact finite difference schemes for computational mechanics*, Ph. D. Thesis, University of Texas at Austin, 1995.

36. Jia R., Yu X., Xing J., Ning Y., and Sun H., An improved method using adaptive smoothing for GNSS tomographic imaging of ionosphere, *PLoS ONE*, 2021, vol. 16, no. 5, e0250613.
https://doi.org/10.1371/journal.pone.0250613